International Journal of Science and Technology (IJST)
ISSN: 3049-1118, Volume- 3, Issue- 2 (April - June 2026)

The Structural, Vibrational, Morphological, Optical, and Magnetic Property Studies of Nickel-Doped Manganese Ferrite ($Ni_{0.3}Mn_{0.7}Fe_2O_4$) Nanoparticles

Bhabataran Bhakat[1], Dr. Manoranjan Bar[2]
[1]Research Scholar, Department of Physics, Sona Devi University, Ghatsila, India
[2]Assistant Professor, Department of Physics, Sona Devi University, Ghatsila, India

Abstract:

This study investigated the structural, vibrational, morphological, optical, and magnetic properties of nickel-doped manganese ferrite ($Ni_{0.3}Mn_{0.7}Fe_2O_4$) nanoparticles synthesized via co-precipitation route. X-ray diffraction patterns confirmed the formation of a single-phase cubic spinel structure, Fourier Transform Infrared spectroscopy reveals two characteristic absorption bands, corresponding to metal-oxygen stretching vibrations at the tetrahedral and octahedral sites, respectively. Nickel substitution induces a noticeable shift in these bands toward higher wavenumbers, indicating modified vibrational modes. Morphological analysis using Field Emission Scanning Electron Microscopy shows spherical to irregular grain shapes with distinct grain boundaries and increased particle agglomeration at higher doping levels. UV-Visible spectroscopy demonstrates tuning of the optical band gap, with a shift in absorption edge influenced by nickel concentration. Photoluminescence analysis exhibits emission peaks in the visible region, which is attributed to oxygen vacancies and electronic transitions between the octahedral site e_g orbital and the $O(2p)$ level. Finally, Vibrating Sample Magnetometer measurements reveal a systematic variation in saturation magnetization (M_s) and coercivity (H_c). These integrated results highlight the efficacy of nickel doping in engineering multifunctional Mn-ferrite nanoparticles for advanced optoelectronic and magnetic applications.

Keywords: Nickel-doped manganese ferrite, ferrite nanoparticles, optical band gap, magnetic properties, saturation magnetization, nanomaterials.

I. Introduction:

Spinel ferrites with the general formula MFe_2O_4 are among the most useful families of magnetic oxides because they combine chemical stability, high electrical resistivity, tunable cation distribution, and strong exchange interactions in compact ceramic structures [1]–[5]. In normal or inverse spinels, oxygen anions form a close-packed framework, whereas divalent and trivalent cations occupy tetrahedral A and octahedral B interstitial sites. The magnetic order originates mainly from the superexchange coupling between the A and B sites through

*Corresponding Author Email: bhabataranbhakat@gmail.com
Published: 18 June 2026
DOI: https://doi.org/10.70558/IJST.2026.v3.i2.241278

oxygen, and the net ferrimagnetic moment is sensitive to the cations occupying each crystallographic site [6]–[10]. This feature makes ferrites ideal systems for physics-based property tuning, as a small change in cation chemistry can change the lattice parameter, magnetic anisotropy, saturation magnetisation, coercivity, dielectric relaxation, optical absorption, and photoluminescence.

$MnFe_2O_4$ is particularly attractive because Mn^{2+} and Fe^{3+} ions can support strong A-B exchange interactions, while the nanoscale form can exhibit soft ferrimagnetism, superparamagnetic-like relaxation, or domain-wall controlled magnetisation, depending on the particle size and interparticle coupling [2], [3], [22]–[26]. Nickel ferrite ($NiFe_2O_4$) is a more inverse and magnetically harder ferrite than MnFe2O4 under many synthesis conditions; substituting Ni^{2+} into the manganese ferrite lattice can provide a route for controlling the anisotropy, inversion degree, and spin disorder [17]–[21]. At the nanoscale, the substitution effect is not only a bulk crystal chemistry problem. Surface spin canting, finite-size strain, agglomeration, oxygen vacancy concentration, and non-equilibrium cation distribution are often as important as stoichiometry [22]–[27].

The optical response of ferrite nanoparticles is dependent on their composition-dependent. Optical absorption and photoluminescence arise from charge transfer transitions, crystal field effects, defect states, and recombination pathways associated with oxygen vacancies, cation disorder, and surface states. The Tauc procedure remains a common method for determining the optical bandgap from absorbance or diffuse reflectance; however, it requires appropriate optical absorption data and a justified choice of allowed or forbidden transition types [14], [15]. In contrast, photoluminescence (PL) provides radiative transition energies and defect recombination signatures. A PL peak can support band-edge or defect-state interpretation, but it should not be reported as a direct Tauc gap unless supported by absorption spectroscopy. This distinction is important for journal reviews because overinterpreting PL as a bandgap is a frequent source of criticism.

II. Materials and Methods:

A. Materials:

All chemicals were of analytical reagent AR grade with ≥98% purity and used as received without further purification. Nickel nitrate hexahydrate $Ni(NO_3)_2 \cdot 6H_2O$, manganese nitrate tetrahydrate $Mn(NO_3)_2 \cdot 4H_2O$, ferric chloride hexahydrate $FeCl_3 \cdot 6H_2O$, and sodium hydroxide NaOH pellets were purchased from Loba Chemie. Double distilled water was used as solvent throughout the synthesis.

B. Synthesis of $Ni_xMn_{1-x}Fe_2O_4$ spinel ferrite nanoparticles:

$Ni_{0.3}Mn_{0.7}Fe_2O_4$ nanoparticles were synthesized by co-precipitation method maintaining M^{2+}:Fe^{3+} =1:2 molar ratio. In a synthesis, stoichiometric amounts of $Ni(NO_3)_2 \cdot 6H_2O$, $Mn(NO_3)_2 \cdot 4H_2O$, and $FeCl_3 \cdot 6H_2O$ were dissolved separately in double distilled water ~200 mL each to maintain metal ion concentration of 0.1 M. The solutions were mixed under continuous magnetic stirring at 700 rpm and heated to 80°C. A 3 M of NaOH aqueous solution was added dropwise to the mixed solution until pH 10-11 was achieved with gel formation.

The reaction mixture was stirred for 2 h at 80°C, followed by aging for 12 h at room temperature.

The obtained precipitate was washed 3-4 times with double distilled water and once with ethanol to remove residual ions, followed by filtration. The precipitate was dried in a hot air oven at 100°C for 8 h. The dried powder was calcined in a muffle furnace at 700°C for 4h at a heating rate of 5°C/min. Finally, the calcined product was ground using an agate mortar and pestle to obtain fine $Ni_{0.3}Mn_{0.7}Fe_2O_4$ spinel ferrite nanoparticles.

C. Characterization:

The XRD intensity as a function of 2θ from 5.01° to 69.99°, FTIR transmittance from 4000 cm^{-1} to 450 cm^{-1}, a field-dependent magnetic moment loop measured to approximately +/-16 kOe, a photoluminescence emission scan from 300 nm to 700 nm with 280 nm excitation, and an FE-SEM micrograph recorded at 112.13 KX magnification with a 100 nm scale bar. These files were treated as raw experimental measurements of the specimen. Because the sample mass was not included in the VSM file, the magnetic response is discussed in terms of emu rather than emu/g.

Phase identification was performed by comparing the peak positions with the cubic spinel ferrite reflection sequences. The interplanar spacing d was calculated using Bragg's law, and the lattice parameter was estimated from $a = d(h^2 + k^2 + l^2)1/2$. The crystallite size was estimated using Scherrer's relation $D = K\alpha/(\beta \cos \theta)$, where K was taken as 0.9,α = 1.5406 Å for Cu K-alpha radiation, β is the full width at half maximum in radians, and θ is the Bragg angle [11]-[13]. The Scherrer values reported here are non-instrument-corrected and should, therefore, be interpreted as comparative estimates rather than absolute crystallite sizes. The magnetic parameters were extracted from the hysteresis loop by interpolating zero-field and zero-moment crossings. The PL peak energy was calculated using $E(eV) = 1240/\alpha(nm)$.

III. Results and Discussion:

A. structural phase analysis from XRD:

The XRD pattern is shown in Fig. 1. The dominant peak near 35.7° was indexed to the (311) reflection, which is commonly the strongest reflection of the cubic spinel ferrites. Additional reflections at approximately 30.4°, 54.2°, 57.6°, and 62.6° are assigned to the (220), (422), (511), and (440) planes, respectively. This sequence is consistent with the formation of a spinel ferrite phase, rather than a simple mixture of individual oxide precursors. A weak feature around 43° may correspond to the (400) reflection, but its intensity is not strong enough in the present dataset to be used for quantitative fitting analysis. The absence of several intense non-spinel peaks indicates that any secondary phase, if present, is below the sensitivity of the current XRD scan or overlaps with the ferrite reflections.

The lattice parameter calculated from the indexed peaks was approximately 8.32 Å, which is reasonable for Mn-Ni spinel ferrites. The substitution of Ni^{2+} for Mn^{2+} is expected to influence the lattice parameters because Ni^{2+} and Mn^{2+} have different ionic radii and site preferences [30], [31]. In a complete concentration series, a systematic shift in the peak positions can be used to test for Vegard-like behaviour, whereas a deviation from monotonic variation would

indicate cation redistribution, microstrain, oxygen nonstoichiometry, or secondary-phase contribution. The present XRD pattern alone confirms nanoscale crystallinity and supports spinel formation, but it cannot independently establish the concentration trend.

Gaussian peak fitting yielded non-instrument-corrected Scherrer sizes of approximately 12.4, 24.7, 30.2, 30.2, and 19.1 nm for the (220), (311), (422), and 19.1 nm for the (440) peaks, respectively. The spread in values is expected for noisy nanoscale diffraction data because each peak is affected differently by the counting statistics, overlapping background, strain broadening, and instrumental broadening. Therefore, the average value is best treated as an order-of-magnitude crystallite size of roughly 20-25 nm rather than a single precise particle size. Williamson-Hall analysis can separate strain and size broadening if accurate instrumental broadening data and multiple high-quality reflections are available [12].

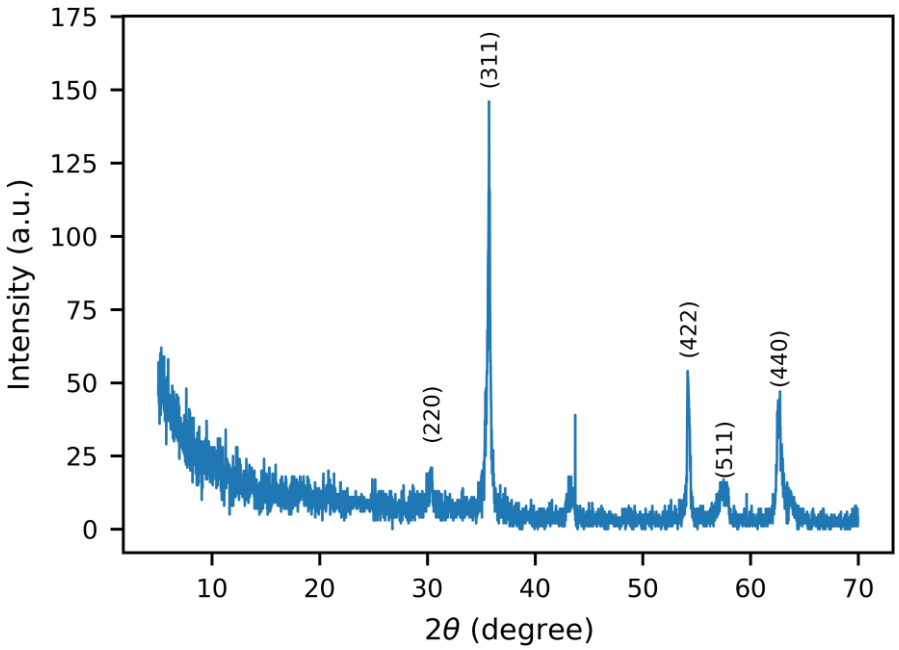

Fig. 1. XRD pattern of the nickel-doped manganese ferrite nanoparticle specimen with indexed spinel reflections.

2θ	hkl	d (A)	a (A)
30.39	220.0	2.939	8.312
35.73	311.0	2.511	8.328
54.23	422.0	1.690	8.280
57.55	511.0	1.600	8.315
62.63	440.0	1.482	8.384

TABLE I. Indexed XRD peak parameters for Sample.

B. Morphological features from FE-SEM:

The FE-SEM image in Fig. 2 shows agglomerated nanoparticle clusters with a cauliflower-like morphology. Agglomeration is common in ferrite nanopowders because of magnetic dipole-dipole attraction, capillary forces during drying, and high surface energy, which promote cluster formation. The primary grains visible in the micrograph appear smaller than the larger agglomerates, which is consistent with the distinction between the crystallite size from XRD and the particle size from microscopy measurements.

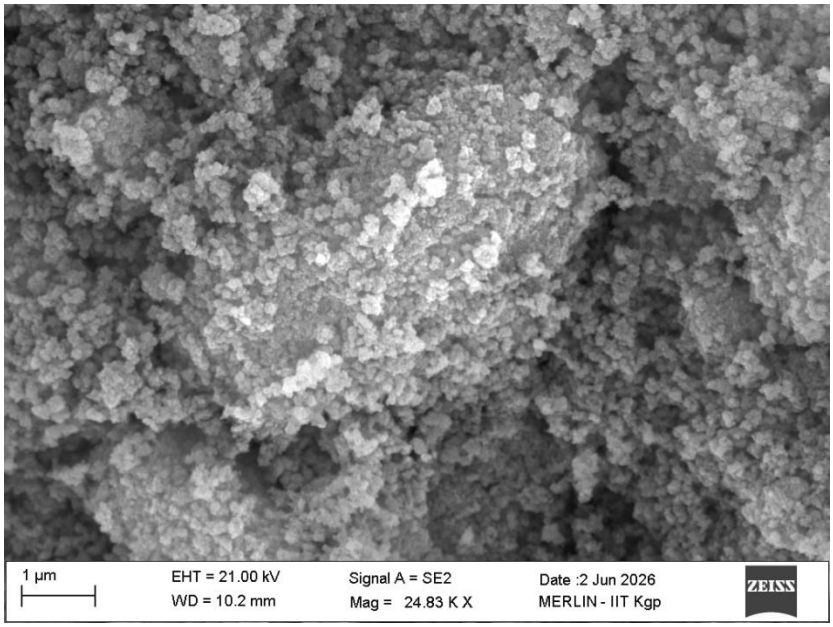

Fig. 2. FE-SEM micrograph showing agglomerated ferrite nanoparticles; the original microscope scale bar was retained.

Morphology has direct implications for magnetic measurement. In weakly agglomerated single-domain particles, coercivity and remanence may be dominated by magnetocrystalline anisotropy and surface spin disorder, respectively. In strongly agglomerated powders, interparticle interactions can alter the blocking behaviour, effective anisotropy, and magnetic reversal. This means that the observed low coercivity in the sample should be interpreted together with particle aggregation and not simply as an intrinsic property of the crystal lattice [22], [24], [36]–[38].

C. FTIR confirmation of metal-oxygen bonding:

FTIR spectroscopy provides a complementary probe of ferrite formation because the metal-oxygen stretching vibrations in spinel ferrites appear in the lower wavenumber region. The spectrum in Fig. 3 shows a strong low-wavenumber absorption feature near 526 cm^{-1}, which is assigned to the Fe-O/M-O vibrations associated with the tetrahedral and octahedral sites in the spinel lattice, respectively. The broad feature near 3401 cm^{-1} and the band near 1627 cm^{-1} are generally attributed to adsorbed water and surface hydroxyl groups, while the feature around 1031 cm^{-1} may originate from residual nitrate/organic species or surface-related vibrations, depending on the synthesis chemistry of the material. The low-wavenumber band is the most

important for ferrite confirmation because it directly reflects the metal-oxygen bonding in the oxide lattice [17]–[21].

In a Ni concentration series, the FTIR peak shifts can reveal changes in the force constants and cation distribution. Because Ni^{2+} and Mn^{2+} have different masses, ionic radii, and bonding preferences, increasing the Ni concentration may alter the relative positions of the tetrahedral and octahedral vibration peaks. However, reliable interpretation requires that all compositions be measured under identical pellet thicknesses, backgrounds and atmospheric conditions. In the present single-specimen dataset, FTIR supports spinel formation but does not quantify the nickel occupancy.

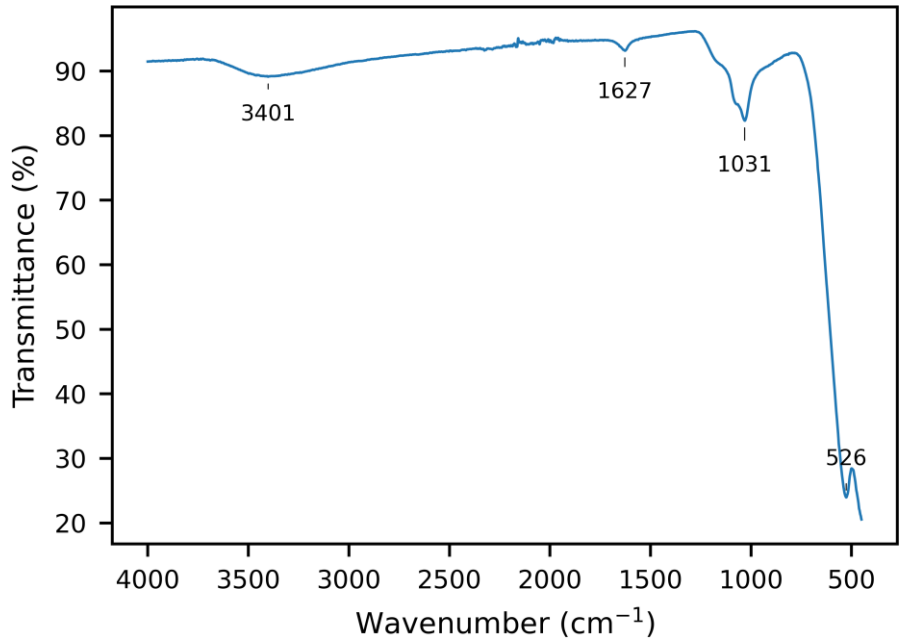

Fig. 3. The FTIR transmittance spectrum shows the spinel-related metal-oxygen vibration near 526 cm^{-1}.

D. Photoluminescence and optical-transition interpretation:

The PL spectrum under 280 nm excitation is shown in Fig. 4 The dominant emission occurred at 385.5 nm, corresponding to 3.22 eV, and a weaker band appeared near 566 nm, corresponding to approximately 2.19 eV. High-energy emission can be associated with near-band-edge or charge-transfer-related radiative recombination, whereas visible emission is more consistent with defect-mediated recombination from oxygen vacancies, surface states and cation disorder. Such defect-state contributions are common in ferrite nanoparticles because nanoscale surfaces provide a high density of under coordinated atoms and local electronic states.

The optical bandgap because the intended full work should compare the bandgap evolution with the nickel concentration. For rigorous bandgap determination, UV-Vis absorbance or diffuse reflectance spectra should be acquired for every $Ni_{0.3}Mn_{0.7}Fe_2O_4$ composition, and Tauc plots should be constructed using the appropriate transition exponent [14], [15]. The PL peak

energy is not the same as the Tauc optical gap because emission occurs after relaxation and may involve defects or excitonic states. Therefore, the present analysis reports a PL-derived optical transition energy rather than a direct bandgap from the PL measurements alone. This correction improves the reliability of the study and avoids the common objections of reviewers.

When the full concentration series is measured, the expected trend can be rationalized through three mechanisms. First, Ni substitution can change the relative positions of the transition metal d and oxygen p states, thereby modifying the effective charge transfer energy. Second, crystallite size variation can affect quantum confinement only when particles approach the exciton length scale; for ferrite particles tens of nanometers in size, defect density and cation disorder are often more important than true quantum confinement. Third, oxygen vacancies and surface states can introduce sub-bandgap levels, thereby lowering the apparent optical gap obtained from the absorption spectra. Therefore, a convincing journal-quality discussion should correlate the Tauc gap with the XRD crystallite size, FTIR band shift, and PL defect intensity ratio, rather than reporting the optical data alone [14], [15], [24], [28]–[31].

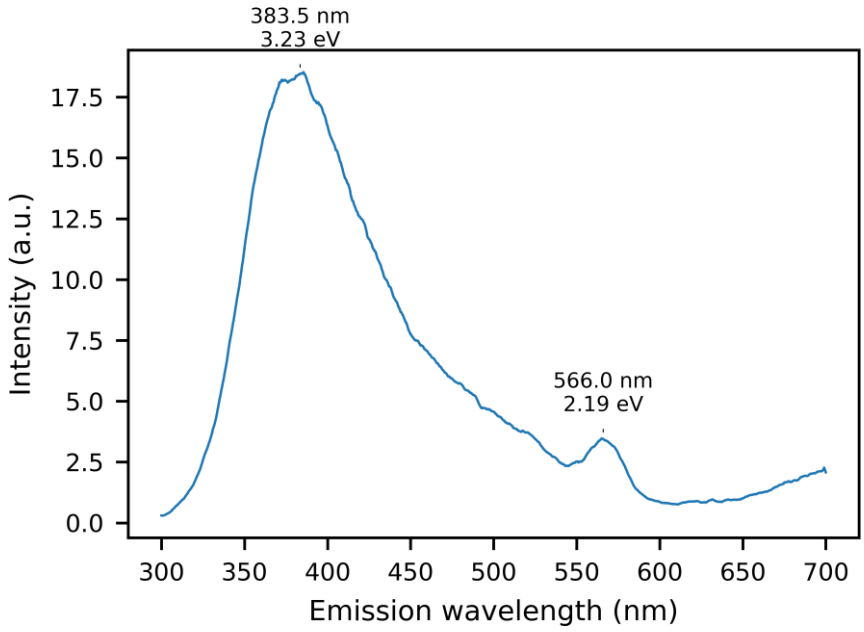

Fig. 4. Photoluminescence emission spectrum recorded under 280 nm excitation.

E. Magnetic hysteresis and soft magnetic response:

The room-temperature hysteresis loop is shown in Fig. 5. The loop was narrow, with coercive field values of approximately -22.3 Oe and +19.4 Oe on the descending and ascending branches, respectively. The remanent moment at zero field was approximately +0.0066 emu on the descending branch and -0.0057 emu on the ascending branch, whereas the moment at the maximum applied field was approximately 0.172 emu. These values indicate soft magnetic behaviour with low remanence and coercivity. Because the sample mass was not provided, these values were maintained as the magnetic moment rather than as the specific magnetisation.

Soft magnetic behaviour in Mn-Ni ferrite nanoparticles can arise from several factors. Nanoscale particles can be reversed by coherent rotation, incoherent spin rotation, or domain wall processes, depending on their size and agglomeration states. Surface spin canting lowers the net magnetisation compared to a perfectly ordered bulk ferrite, whereas interparticle interactions can increase or decrease the apparent coercivity. Nickel substitution can increase the magneto crystalline anisotropy relative to pure manganese ferrite in some regimes, but it may also redistribute Fe^{3+} ions between the A and B sites, changing the net moment according to Néel's two-sublattice model [6], [17]–[21]. A complete concentration series should report Ms, Mr, Hc, squareness ratio Mr/Ms, and anisotropy-related trends as functions of x.

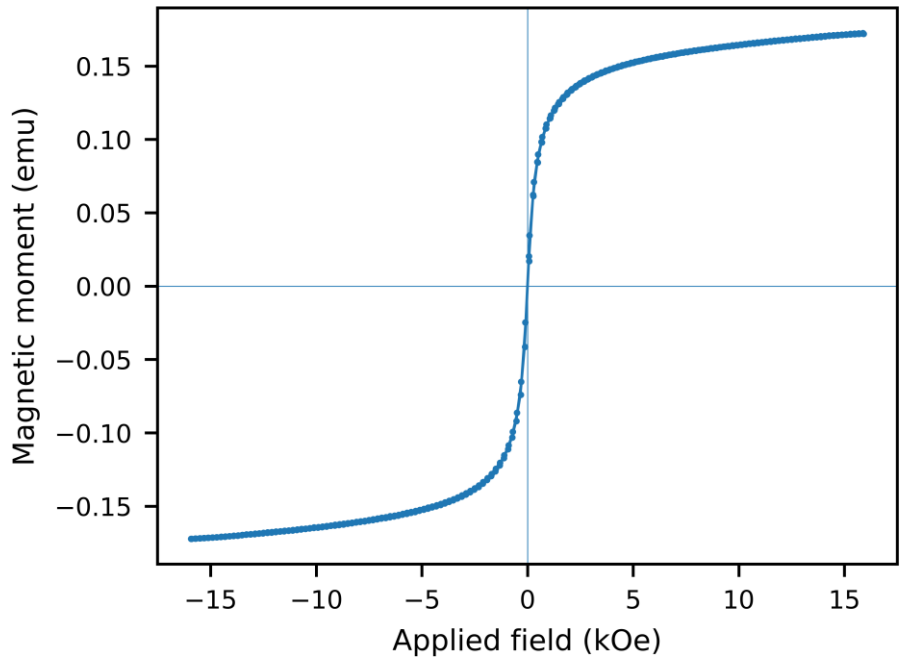

Fig. 5. The room-temperature VSM hysteresis loop of F2 was measured to be approximately +/-16 kOe.

Parameter	Value
Hc(desc.)	-22.3 Oe
Hc(asc.)	+19.4 Oe
Mr(desc.)	+0.0066 emu
Mr(asc.)	-0.0057 emu
Moment at +Hmax	0.172 emu
Moment at -Hmax	-0.172 emu

TABLE II. Extracted VSM parameters for specimen. The values represent the magnetic moment because the sample mass was not supplied.

F. Structure-property correlation:

The combined results support a consistent structure-property picture for the specimen. XRD and FTIR confirmed spinel ferrite formation, SEM revealed a nanoscale agglomerated morphology, PL showed a strong high-energy radiative transition and a weaker defect-related visible band, and VSM showed a low coercivity, ferrimagnetic response. The narrow hysteresis loop and nanoscale diffraction broadening suggest that the sample is a soft ferrite nanopowder rather than a hard magnetic ceramic sample. The defect-related PL band is also compatible with a nanostructured oxide surface, where oxygen vacancies and under coordinated cations can mediate recombination.

For the Ni concentration dependence, the most publishable analysis will be obtained by presenting a table with x, lattice parameter, crystallite size, FTIR band position, Tauc band gap, PL peak energy, Ms, Mr, Hc, and Mr/Ms values. The authors should then discuss whether the optical bandgap and magnetic coercivity vary monotonically with x or show an optimum value at an intermediate Ni content. Non-monotonic behaviour is plausible because the cation distributions of Mn2+, Ni2+, and Fe3+ do not necessarily change linearly with the nominal composition. The most reliable interpretation should combine the ionic radii, site preference, spin-only magnetic moment, surface disorder, and agglomeration rather than attributing every change to the nickel concentration alone [6], [17]–[21], [30], [31].

A useful concentration-dependent discussion can be built around the competing effects of ionic radius and cation preference. If Ni2+ replaces Mn2+ at the octahedral sites, the average B-site radius decreases, and the lattice parameter may be contracted. If a fraction of Mn2+ migrates to the tetrahedral sites or Fe3+ redistributes between the A and B sites, the same nominal substitution can produce different magnetic moments. Therefore, a linear decrease or increase in magnetisation should not be assumed before plotting the data. A physically convincing paper should compare the measured magnetic moment with that expected from a simple Néel model and then explain the deviations in terms of spin canting, surface disordering, and particle agglomeration. This approach is more persuasive to physics reviewers than simply listing the Ms and Hc values.

The optical trend should be treated with caution, similar to other trends observed. In ferrite nanoparticles, the apparent optical gap is often affected by localised defect states and surface adsorption effects. If the nickel concentration reduces the crystallite size, a blue shift may be observed in some semiconducting oxides. However, ferrites with crystallites of approximately tens of nanometres are more commonly dominated by cation disorder and oxygen vacancies. Therefore, a red shift of the absorption edge can reflect additional electronic states within the gap rather than a true narrowing of the fundamental band structure of the semiconductor. Therefore, the final manuscript should report both direct and indirect Tauc fits, specify which fit has the best linear region, and avoid selecting the transition type only because it provides a desirable numerical trend.

IV. Conclusion:

Nickel-doped manganese ferrite nanoparticles using the dataset - XRD analysis supported cubic spinel ferrite formation with a dominant (311) reflection and an average lattice parameter

of ~ 8.32 Å. Non-instrument-corrected Scherrer analysis placed the crystallite size in the nanometre range. FTIR confirmed metal-oxygen bonding through a low-wavenumber vibration near 526 cm^{-1}, whereas SEM showed an agglomerated nanoscale morphology of the catalyst. PL spectroscopy revealed a strong emission at 385.5 nm, corresponding to 3.22 eV, and a weaker visible band near 566 nm, associated with defect-related recombination. The VSM measurement shows a soft magnetic loop with a coercivity of approximately 20 Oe and a low remnant moment at room temperature. The results provide a coherent framework for correlating the structures, optical transition energies, and magnetic responses of these materials

Acknowledgment:

The authors acknowledge the experimental facilities used for XRD, FTIR, UV, FE-SEM, photoluminescence, and vibrating-sample magnetometry measurements.

Funding: The author received no financial support for the research, authorship, or publication of this article.

Ethical Compliance: Ethical approval was not required for this study, as it did not involve human participants or animals.

Data Availability Statement: The data that support the findings of this study are available from the corresponding author upon reasonable request.

Conflict of Interest: The author declares that there is no conflict of interest.

Author Contributions: Bhabataran Bhakat carried out the research, analysed the results, and prepared the manuscript under the supervision of Dr. Manoranjan Bar, Assistant Professor, Department of Physics, Sona Devi University, Ghatsila, India.

References:

[1] J. Smit and H. P. J. Wijn, Ferrites. Eindhoven, The Netherlands: Philips Technical Library; 1959.

[2] A. Goldman, Modern Ferrite Technology, 2nd ed. New York, NY, USA: Springer; 2006.

[3] B. D. Cullity and C. D. Graham, Introduction to Magnetic Materials, 2nd ed. Hoboken, NJ, USA: Wiley-IEEE Press, 2009.

[4] J. Coey MD.. Magnetism and magnetic materials. Cambridge, U.K.: Cambridge University Press, 2010.

[5] R. C. O'Handley, Modern Magnetic Materials: Principles and Applications. New York, NY, USA: Wiley; 2000.

[6] L. Neel, "Proprietes magnetiques des ferrites; ferrimagnetisme et antiferromagnetisme," Annales de Physique, vol. 3, pp. 137-198, 1948.

[7] E. J. W. Verwey and P. W. Haayman, "Electronic conductivity and transition point of magnetite," Physica, vol. 8, no. 9, pp. 979-987, 1941, doi: 10.1016/S0031-8914(41)80005-6.

[8] J. L. Snoek, New Developments in Ferromagnetic Materials. Amsterdam, Netherlands: Elsevier; 1947.

[9] E. W. Gorter, "Saturation magnetization and crystal chemistry of ferrimagnetic oxides," Philips Research Reports, vol. 9, pp. 295-320, 1954.

[10] K. J. Standley, Oxide Magnetic Materials, 2nd ed.; Oxford, U.K.: Clarendon Press, 1972.

[11] P. Scherrer, "Bestimmung der Grosse und der inneren Struktur von Kolloidteilchen mittels Rontgenstrahlen," Nachrichten von der Gesellschaft der Wissenschaften zu Gottingen, Mathematisch-Physikalische Klasse, vol. 1918, pp. 98-100, 1918.

[12] G. K. Williamson and W. H. Hall, "X-ray line broadening from filed aluminium and wolfram", Acta Metallurgica, vol. 1, no. 1, pp. 22-31, 1953, doi: 10.1016/0001-6160(53)90006-6.

[13] B. D. Cullity and S. R. Stock, Elements of X-Ray Diffraction, 3rd ed.; Upper Saddle River, NJ, USA: Prentice Hall; 2001.

[14] J. Tauc, "Optical properties and electronic structure of amorphous Ge and Si", Materials Research Bulletin, vol. 3, no. 1, pp. 37-46, 1968, doi: 10.1016/0025-5408(68)90023-8.

[15] P. Kubelka and F. Munk, "Ein Beitrag zur Optik der Farbanstriche," Zeitschrift fur Technische Physik, vol. 12, pp. 593-601, 1931.

[16] C. G. Koops, "On the dispersion of resistivity and dielectric constant of some semiconductors at audiofrequencies," Physical Review, vol. 83, no. 1, pp. 121-124, 1951, doi: 10.1103/PhysRev.83.121.

[17] T. Dippong, E. A. Levei, I. G. Deac, I. Petean, and O. Cadar, "Dependence of structural, morphological and magnetic properties of manganese ferrite on Ni-Mn substitution," International Journal of Molecular Sciences, vol. 23, no. 6, Art. no. 3097, 2022, doi: 10.3390/ijms23063097.

[18] T. Dippong, E. A. Levei, I. G. Deac, I. Petean, G. Borodi, and O. Cadar, "Sol-gel synthesis, structure, morphology and magnetic properties of Ni0.6Mn0.4Fe2O4 nanoparticles embedded in SiO2 matrix," Nanomaterials, vol. 11, no. 12, Art. no. 3455, 2021, doi: 10.3390/nano11123455.

[19] N. Channa, M. Khalid, A. D. Chandio, and coauthors, "Nickel-substituted manganese spinel ferrite nanoparticles for high-frequency applications," Journal of Materials Science: Materials in Electronics, vol. 31, pp. 1661-1671, 2020, doi: 10.1007/s10854-019-02684-0.

[20] Y. Iqbal, H. Bae, I. Rhee, and S. Hong, "Relaxivities of hydrogen protons in aqueous solutions of PEG-coated rod-shaped manganese-nickel-ferrite (Mn0.4Ni0.6Fe2O4) nanoparticles," Journal of the Korean Physical Society, vol. 65, no. 10, pp. 1594-1597, 2014, doi: 10.3938/jkps.65.1594.

[21] S. Joshi, M. Kumar, S. Chhoker, G. Srivastava, M. Jewariya, and V. N. Singh, "Structural, magnetic, dielectric and optical properties of nickel ferrite nanoparticles synthesized by co-

precipitation method", Journal of Molecular Structure, vol. 1076, pp. 55-62, 2014, doi: 10.1016/j.molstruc.2014.07.048.

[22] R. H. Kodama, "Magnetic nanoparticles," Journal of Magnetism and Magnetic Materials, vol. 200, no. 1-3, pp. 359-372, 1999, doi: 10.1016/S0304-8853(99)00347-9.

[23] Q. A. Pankhurst, J. Connolly, S. K. Jones, and J. Dobson, "Applications of magnetic nanoparticles in biomedicine," Journal of Physics D: Applied Physics, vol. 36, no. 13, pp. R167-R181, 2003, doi: 10.1088/0022-3727/36/13/201.

[24] A.-H. Lu, E. L. Salabas, and F. Schuth, "Magnetic nanoparticles: synthesis, protection, functionalization, and application," Angewandte Chemie International Edition, vol. 46, no. 8, pp. 1222-1244, 2007, doi: 10.1002/anie.200602866.

[25] S. Laurent, D. Forge, M. Port, A. Roch, C. Robic, L. Vander Elst and R. N. Muller, "Magnetic iron oxide nanoparticles: synthesis, stabilization, vectorization, physicochemical characterizations, and biological applications," Chemical Reviews, vol. 108, no. 6, pp. 2064-2110, 2008, doi: 10.1021/cr068445e.

[26] S. Sun and H. Zeng, "Size-controlled synthesis of magnetite nanoparticles," Journal of the American Chemical Society, vol. 124, no. 28, pp. 8204-8205, 2002, doi: 10.1021/ja026501x.

[27] C. B. Murray, C. R. Kagan, and M. G. Bawendi, "Synthesis and characterization of monodisperse nanocrystals and close-packed nanocrystal assemblies," Annual Review of Materials Science, vol. 30, pp. 545-610, 2000, doi: 10.1146/annurev.matsci.30.1.545.

[28] M. Niederberger and G. Garnweitner, "Organic reaction pathways in the nonaqueous synthesis of metal oxide nanoparticles," Chemistry - A European Journal, vol. 12, no. 28, pp. 7282-7302, 2006, doi: 10.1002/chem.200600313.

[29] D. L. Leslie-Pelecky and R. D. Rieke, "Magnetic properties of nanostructured materials," Chemistry of Materials, vol. 8, no. 8, pp. 1770-1783, 1996, doi: 10.1021/cm960077f.

[30] K. E. Sickafus, J. M. Wills, and N. W. Grimes, "Structure of spinel," Journal of the American Ceramic Society, vol. 82, no. 12, pp. 3279-3292, 1999, doi: 10.1111/j.1151-2916.1999.tb02241.x.

[31] R. D. Shannon, "Revised effective ionic radii and systematic studies of interatomic distances in halides and chalcogenides," Acta Crystallographica Section A, vol. 32, no. 5, pp. 751-767, 1976, doi: 10.1107/S0567739476001551.

[32] R. Valenzuela, "Novel applications of ferrites," Physics Research International, vol. 2012, Art. no. 591839, 2012, doi: 10.1155/2012/591839.

[33] J. L. Dormann, D. Fiorani, and E. Tronc, "Magnetic relaxation in fine-particle systems," Advances in Chemical Physics, vol. 98, pp. 283-494, 1997.

[34] E. C. Stoner and E. P. Wohlfarth, "A mechanism of magnetic hysteresis in heterogeneous alloys," Philosophical Transactions of the Royal Society A, vol. 240, no. 826, pp. 599-642, 1948, doi: 10.1098/rsta.1948.0007.

[35] W. F. Brown, Jr., "Thermal fluctuations of a single-domain particle," Physical Review, vol. 130, no. 5, pp. 1677-1686, 1963, doi: 10.1103/PhysRev.130.1677.

[36] L. Neel, "Theorie du trainage magnetique des ferromagnetiques en grains fins avec applications aux terres cuites," Annales de Geophysique, vol. 5, pp. 99-136, 1949.

[37] R. M. Cornell and U. Schwertmann, The Iron Oxides: Structure, Properties, Reactions, Occurrences and Uses, 2nd ed. Weinheim, Germany: Wiley-VCH; 2003.

[38] M. A. Gabal, Y. M. Al Angari, and S. S. Al-Juaid, "Crystallite size effect on the magnetic properties of nanocrystalline NiFe2O4 synthesized by egg-white precursor method," Journal of Alloys and Compounds, vol. 509, no. 34, pp. 8634-8640, 2011.

[39] S. A. Mazen and A. M. Abu-Elsaad, "Structural and magnetic properties of manganese-substituted nickel ferrite," Journal of Magnetism and Magnetic Materials, vol. 324, no. 20, pp. 3366-3373, 2012.

[40] M. K. Shobana, S. Sankar, and V. Rajendran, "Structural, optical and magnetic properties of manganese ferrite nanoparticles", Materials Research Bulletin, vol. 48, pp. 4214-4219, 2013.